The small EF-hand protein CALML4 functions as a critical myosin light chain within the intermicrovillar adhesion complex

Received for publication, January 27, 2020, and in revised form, March 18, 2020 Published, Papers in Press, March 24, 2020, DOI 10.1074/jbc.RA120.012820

Myoung Soo Choi[‡], Maura J. Graves[‡], Samaneh Matoo[‡], Zachary A. Storad[‡], Rawnag A. El Sheikh Idris[‡], Meredith L. Weck[§], Zachary B. Smith[§], Matthew J. Tyska[§], and Scott W. Crawley[‡1]

From the [‡]Department of Biological Sciences, University of Toledo, Toledo, Ohio 43606 and the [§]Department of Cell and Developmental Biology, Vanderbilt University School of Medicine, Nashville, Tennessee 37240

Edited by Enrique M. De La Cruz

Specialized transporting and sensory epithelial cells employ homologous protocadherin-based adhesion complexes to remodel their apical membrane protrusions into organized functional arrays. Within the intestine, the nutrient-transporting enterocytes utilize the intermicrovillar adhesion complex (IMAC) to assemble their apical microvilli into an ordered brush border. The IMAC bears remarkable homology to the Usher complex, whose disruption results in the sensory disorder type 1 Usher syndrome (USH1). However, the entire complement of proteins that comprise both the IMAC and Usher complex are not yet fully elucidated. Using a protein isolation strategy to recover the IMAC, we have identified the small EF-hand protein calmodulin-like protein 4 (CALML4) as an IMAC component. Consistent with this finding, we show that CALML4 exhibits marked enrichment at the distal tips of enterocyte microvilli, the site of IMAC function, and is a direct binding partner of the IMAC component myosin-7b. Moreover, distal tip enrichment of CALML4 is strictly dependent upon its association with myosin-7b, with CALML4 acting as a light chain for this myosin. We further show that genetic disruption of CALML4 within enterocytes results in brush border assembly defects that mirror the loss of other IMAC components and that CALML4 can also associate with the Usher complex component myosin-7a. Our study further defines the molecular composition and protein-protein interaction network of the IMAC and Usher complex and may also shed light on the etiology of the sensory disorder USH1H.

Transporting and sensory epithelial cells construct elaborate arrays of actin-based membrane protrusions on their apical surfaces that allow them to interact with the external environment and mediate their specific physiological functions. Prime examples of this can be seen with transporting enterocytes of the intestine and sensory hair cells of the inner ear. Intestinal enterocytes construct a brush border (BB):[2] a densely packed collection of apical microvilli that are enriched in nutrient-processing and transport channels (1). Sensory hair cells assemble an apical hair bundle: a staircase-like array of specialized microvilli, known as stereocilia, that decode sound information into neural signals (2). It has recently become appreciated that these epithelia use adhesion as a conserved mechanism to create and maintain the exquisite order of their apical membrane protrusions (1, 3). In each case, protocadherin-based adhesion is used to create physical linkages that connect neighboring protrusions together, thereby promoting the desire apical architecture. Two homologous protocadherin adhesion complexes generate these physical adhesion links. The IMAC is utilized by transporting epithelia, whereas the "Usher complex" functions in sensory epithelia.

Despite serving tissues with divergent physiological functions, the IMAC and Usher complex exhibit striking homology in both their composition and interactome. The IMAC is comprised of the adhesions molecules CDHR2 (also known as protocadherin-24) and CDHR5 (also known as mucin-like or μ-protocadherin), the PDZ-based scaffold USH1C (also known as harmonin), the ankyrin repeat scaffold ANKS4B, and the myosin motor protein myosin-7b (Myo7b) (4, 5). In the intestine, these proteins target to the distal tips of enterocyte microvilli, where they create intermicrovillar adhesion links that physically couple neighboring microvilli together. During the intermediate stages of BB assembly, intermicrovillar adhesion results in microvilli clustering together on the apical surface. This adhesion between neighbors ultimately results in the assembly of microvilli into highly organized, tightly packed hexagonal arrays that cover the entire apical surface of the mature enterocyte.

This work was supported by a National Science Foundation NOA-AGEP fellowship (to M. J. G.), FYSRE and URSCAP University of Toledo scholarships (to Z. A. S. and R. A. E.), University of Toledo start-up funds, and National Institutes of Health Grants R15GM131382 (to S. W. C.) and DK075555 and DK095811 (to M. J. T.). The authors declare that they have no conflicts of interest with the contents of this article. The content is solely the responsibility of the authors and does not necessarily represent the official views of the National Institutes of Health.
This article was selected as one of our Editors' Picks.
This article contains Figs. S1–S7.

[1] To whom correspondence should be addressed: College of Natural Sciences and Mathematics, University of Toledo, 2801 W. Bancroft St., Toledo, OH 43606. E-mail: william.crawley@utoledo.edu.

[2] The abbreviations used are: BB, brush border; IMAC, intermicrovillar adhesion complex; GST, glutathione *S*-transferase; USH1, type 1 Usher syndrome; ED, ectodomain; EC, extracellular cadherin; EGFP, enhanced GFP; KD, knockdown; KO, knockout; aa, amino acids; CD, cytoplasmic domain; BisTris, 2-[bis(2-hydroxyethyl)amino]-2-(hydroxymethyl)propane-1,3-diol; GAPDH, glyceraldehyde-3-phosphate dehydrogenase; RACE, rapid amplification of cDNA ends.

The Usher complex is comprised of the adhesions molecules cadherin-23 (CDH23) and protocadherin-15 (PCDH15), the scaffolds USH1C and USH1G (also known as Sans), and the motor myosin-7a (Myo7a) (6). Importantly, the USH1C scaffold is shared genetically between the IMAC and Usher complex, although different splice isoforms are utilized between these two complexes (4). The Usher complex has been principally characterized in the inner ear, where it forms "tip-links" that connect adjacent stereocilia on the surface of mechanosensory hair cells (7). More recently, it has been proposed that the Usher complex also plays a role in organizing the actin-based microvilli-like calyceal processes that span the inner and outer segments of photoreceptor cells (8, 9). Genetic disruption of components of the Usher complex results in type 1 Usher syndrome (USH1), a form of severe deafness-blindness in humans (10–16). Depending on which component of the Usher complex is mutated, patients are classified as having a different variant of USH1 (*e.g.* patients with deleterious genetic defects in Myo7a suffer from USH1B). Of note, the causative genes for three USH1 subtypes (USH1E, USH1K, and USH1H) still have not been identified, suggesting that more Usher complex components may remain to be discovered (17–19). A similar situation is seen with the IMAC; structure-function studies of this complex clearly point toward the idea that the full interactome is not yet known (5, 20, 21).

In this study, we sought to further elucidate the molecular composition of the IMAC. To that end, we devised a protein isolation strategy to recover components of the complex associated with CDHR2 and have identified the small EF-hand protein calmodulin-like protein 4 (CALML4) as an additional adhesion complex factor. CALML4 shares 45% sequence identity with conventional calmodulin; however, the functional properties of CALML4 have not been studied to-date. Our interactome analysis suggests that CALML4 incorporates into the IMAC by functioning as a light chain for Myo7b. Given the striking homology between the IMAC and Usher complex, this led us to test and demonstrate that CALML4 is a direct binding partner for the Usher complex motor, Myo7a. In sum, our results suggest that CALML4 may represent the second adhesion complex component that is shared genetically between the IMAC and the Usher complex and therefore may play an important role in both gut and inner ear biology.

Results

Recovery strategy for the CDHR2-associated cytoplasmic complex

The ability of CDHR2 to promote BB assembly depends on its interaction with an ill-defined cytosolic complex that is necessary for both proper targeting and function of the cadherin at the distal tips of enterocyte microvilli (4). Toward the goal of identifying additional components of the IMAC, we devised a protein isolation strategy to recover endogenous CDHR2 and its cytoplasmic complex from enterocyte BBs. We reasoned that we could use the innate adhesion of the IMAC protocadherins as a mechanism to affinity isolate CDHR2. Similar techniques have been used to dissect signaling pathways that are activated by mechanical tension applied to cells (22). Within the BB, CDHR2 and CDHR5 reside at the microvillar tips and interact to form "intermicrovillar adhesion links" that physically couple neighboring microvilli together (4). Our protocol involves incubating magnetic beads coated with the ectodomain (ED) of CDHR5 with isolated BBs to affinity-purify CDHR2. BB-bead incubation is first done in the absence of calcium, a condition under which intermicrovillar adhesion links are disrupted. A calcium switch is then performed to induce adhesion bond formation between the beads and endogenous CDHR2 (Fig. 1*A*). Subsequently, CDHR2 and its associated cytoplasmic complex are recovered using a typical bead-based protein pulldown protocol. The power of this recovery strategy is 2-fold; it exploits the inherent specificity encoded in the *trans*-heterophilic adhesion mediated between the CDHR2 and CDHR5 as an affinity purification step while also benefitting from the fact that the source material used for the purification, namely isolated enterocyte BBs, is highly enriched in the IMAC.

BB isolation does not disrupt IMAC localization

Successful recovery of the CDHR2 cytoplasmic complex using our strategy rests on two principal caveats: that the cytoplasmic complex associated with CDHR2 remains intact during the preparation of our BB source material and that our CDHR5 ED–coated beads are able to make functional interactions with endogenous CDHR2 found in BB microvilli. To begin to test the feasibility of our approach, we first assessed whether the IMAC remains intact in isolated BB source material. Whereas previous proteomic analysis of isolated mouse enterocyte BBs revealed the presence of all known IMAC components (23), it is unclear whether the cytoplasmic complex associated CDHR2 remains intact after BB preparation. To assess the integrity of the CDHR2 cytoplasmic complex, native BBs were isolated from rat small intestinal tissue and stained for USH1C (Fig. 1, *B* and *C*). The scaffold USH1C serves as an excellent marker to assess the CDHR2-associated cytoplasmic complex, as it directly interacts with CDHR2, ANKS4B, and Myo7b and has been shown to be essential for proper distal tip localization of both ANKS4B and Myo7b (4, 5). Confocal imaging of rat BBs stained for USH1C revealed marked enrichment of this scaffold at the distal tips of microvilli, the normal site of IMAC function (Fig. 1*C*). We also sometimes observed signal at the base of the BB microvilli in the region containing the presumptive terminal web, although this staining was also seen in our secondary antibody control and staining for other IMAC components, suggesting that it is nonspecific binding (see CDHR5 BB staining (Fig. S1*A*) and secondary antibody control (Fig. S1*F*)). We further investigated the integrity of the CDHR2-associated complex using BBs isolated from polarized CACO-2_{BBE} cells, an enterocyte model system that uses the IMAC to construct near tissue-like BBs after an extended period in cell culture (4, 24). Similar to the localization of USH1C in BBs isolated from native intestinal tissue, we observed striking examples of USH1C, CDHR2, ANKS4B, and Myo7b at the distal tips of microvilli derived from this polarized cell line (Fig. S1, *B–E*). Thus, in line with previous proteomic data (23), our localization studies suggest that the CDHR2 cytoplasmic complex remains intact at the distal tips of microvilli from isolated BBs.

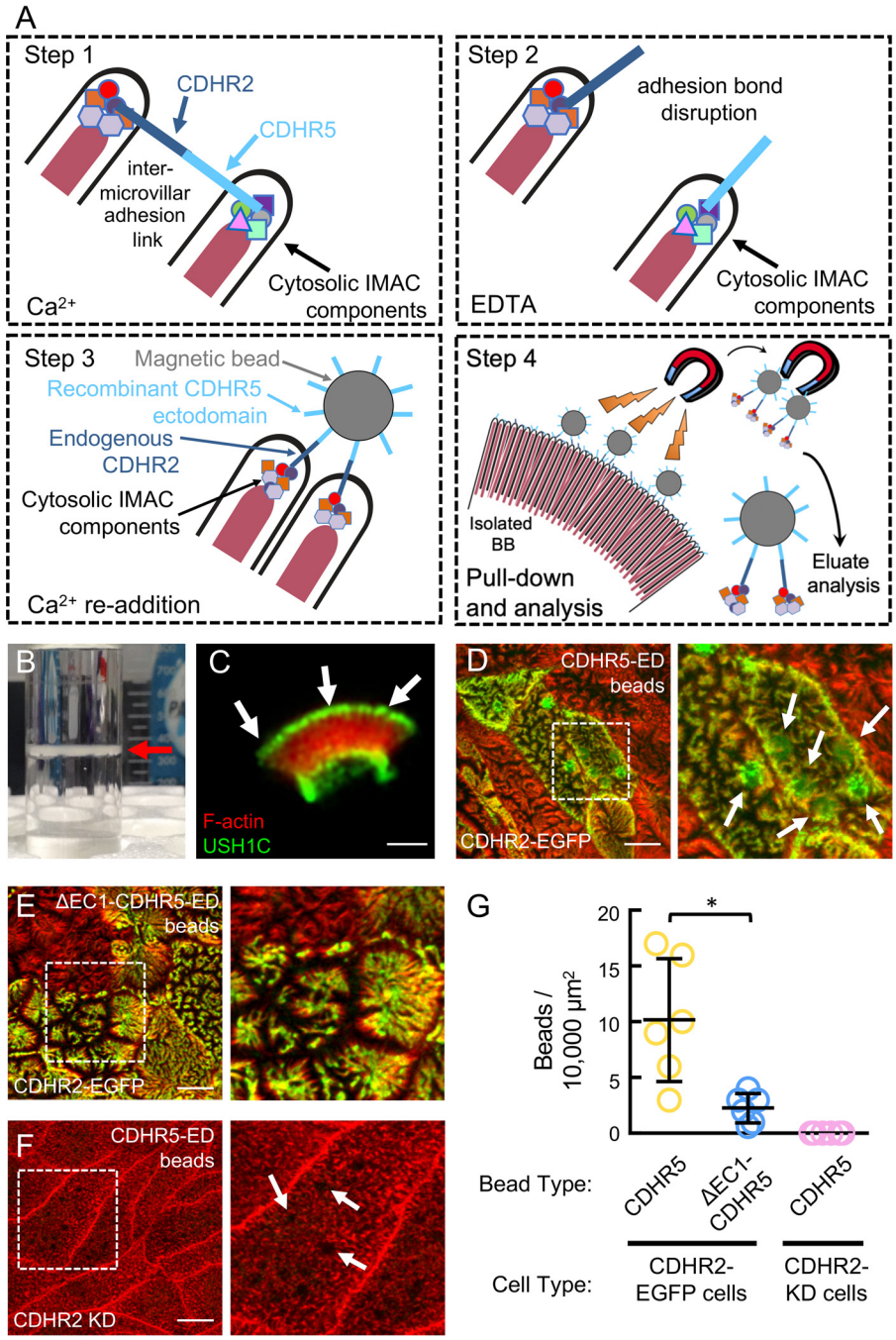

Figure 1. Validation of the strategy used to recover the CDHR2-associated cytoplasmic complex from isolated BBs. *A*, recovery strategy for the CDHR2-associated cytoplasmic complex. See "Results" for details. *B*, purified BBs isolated from rat intestinal tissue. The *red arrow* points to the band of purified BBs found at the 40–60% sucrose gradient interface from the final equilibrium density gradient centrifugation step. *C*, isolated rat BB stained for F-actin (*red*) and USH1C (*green*). The *arrows* point to USH1C at the distal tips of BB microvilli. *Scale bar*, 2 μm. *D* and *E*, CACO-2_{BBE} monolayers stably expressing EGFP-CDHR2 that were incubated with either CDHR5 ED– or ΔEC1-CDHR5–coated beads. *Green*, EGFP-CDHR2; *red*, F-actin. *Boxed regions* denote area in *zooms*. The *arrows* point to beads. Average bead diameter was ~3 μm. *Scale bars*, 10 μm. *F*, CDHR2 KD CACO-2_{BBE} monolayer incubated with CDHR5 ED–coated beads. The *boxed region* denotes the area in *zoom*. The *arrows* point to bead-shaped areas devoid of microvilli. *Scale bar*, 10 μm. *G*, quantification of beads remaining on the cell surface under various experimental conditions. Each data point is derived from a different field of view that has been normalized to an area of 10,000 μm^2. Different fields of view were imaged across three coverslips generated by three independent experiments. Total areas quantified were as follows: for CDHR2-EGFP monolayers, CDHR5 ED beads (47,000 μm^2) and ΔEC1-CDHR5 (45,000 μm^2); for CDHR2 KD monolayers, CDHR5 ED beads (47,000 μm^2). *, $p < 0.01$, *t* test. *Error bars*, S.D.

CDHR5 ED–coated beads associate with BB microvilli

Human CDHR5 exhibits robust heterophilic interaction with CDHR2, with little CDHR5 homophilic adhesion detected using both bead aggregation assays and conventional protein pull-downs (4). We next assessed whether CDHR5 ED–coated beads could make functional interactions with BB microvilli. To this end, we utilized a CACO-2_{BBE} cell line stably expressing CDHR2-EGFP, which served as a marker for the IMAC. CDHR2-EGFP CACO-2_{BBE} cells were allowed to polarize for 6 days, after which CDHR5 ED–coated beads were added to the

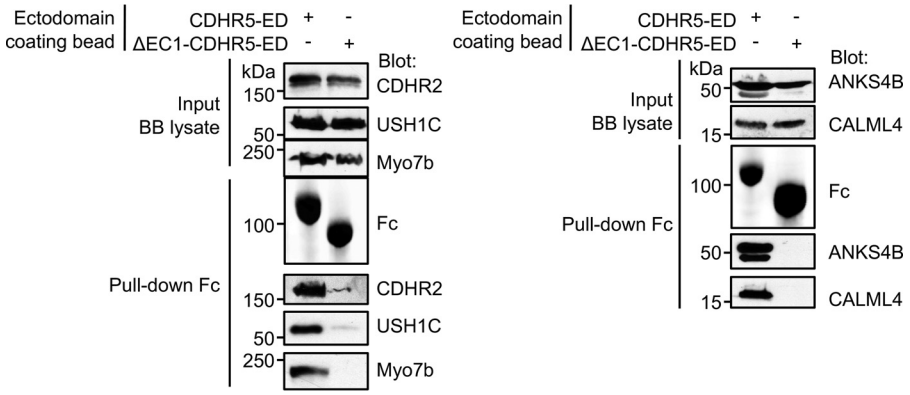

Figure 2. CALML4 is recovered as part of the CDHR2 cytoplasmic complex. Immunoblot analysis of the eluate recovered from incubating CDHR5 ED– or ΔEC1-CDHR5–coated beads with isolated BBs derived from polarized CACO-2_{BBE} monolayers. Amount of sample loaded were 1% for input blots and 20% for eluate blots.

apical surface and cells were allowed to polarize an additional 6 days. As a control, beads coated with the ED of CDHR5 lacking the first extracellular cadherin (EC) domain (ΔEC1-CDHR5 ED) were also seeded onto CDHR2-EGFP CACO-2_{BBE} cells. Adhesion between CDHR5 and CDHR2 was previously shown to be strictly dependent upon the first EC domain within the ectodomain of both cadherins (4). These CACO-2_{BBE} monolayers were then washed extensively while being held at a 90° angle in a coverslip rack to remove unbound beads. Cells were subsequently fixed, stained for F-actin, and visualized by confocal microscopy. We observed abundant examples of BB microvilli forming intimate contact with the CDHR5 ED–coated beads, especially cells in the monolayer overexpressing CDHR2-EGFP (Fig. 1, *D* and *G*). In most cases, BB microvilli seemed to be drawn toward and directly attached to the beads (Fig. S1*G*). We confirmed this using scanning EM, which showed clear examples of microvilli directly bound to beads (Fig. S1*H*). In stark contrast, monolayers that were seeded with ΔEC1-CDHR5 ED–coated beads were largely devoid of beads after extensive washing (Fig. 1, *E* and *G*).

To ensure that the interaction of our CDHR5 ED–coated beads with microvilli was solely dependent upon interaction with CDHR2 (and not some unknown CDHR5-adhesive binding partner), we incubated our beads with polarized CACO-2_{BBE} cells lacking endogenous CDHR2. Microvilli from CDHR2 KD CACO-2_{BBE} failed to retain CDHR5 ED–coated beads (Fig. 1, *F* and *G*). Interestingly, we noted the appearance of "bead-shaped" voids of space lacking microvilli on the apical surface of these CDHR2 KD cells. However, CDHR2 KD cells that were not incubated with beads also displayed identical structures, demonstrating that these voids are not a result of the application of the beads themselves (compare Fig. 1*F* with Fig. S2*A*). In sum, we conclude that CDHR5 ED–coated beads are able to form functional adhesion bonds with native BB microvilli in a manner dependent upon interaction with CDHR2.

Identification of CALML4 as a CDHR2 cytoplasmic complex component

We proceeded by incubating BBs isolated from polarized CACO-2_{BBE} monolayers with CDHR5 ED–coated beads for our IMAC recovery strategy. We chose to utilize BBs derived from CACO-2_{BBE} cells because we had previously validated specific antibodies toward each IMAC component using this cell line that work well for both immunofluorescence and immunoblot analysis, and CACO-2_{BBE} cells can also be genetically manipulated for control experiments. BBs were incubated with CDHR5 ED–coated beads first in the absence of calcium for 20 min, after which a calcium switch step was performed to engage adhesion between the BBs and the beads. As a control, we utilized beads that had been coated with ΔEC1-CDHR5 ED. Beads were subsequently recovered, washed with extraction buffer, eluted with SDS sample buffer, and subjected to immunoblot analysis for the known IMAC components. We confirmed that CDHR2, USH1C, Myo7b, and ANKS4B were all recovered using CDHR5 ED–coated beads, consistent with these components forming a stable complex in BBs (Fig. 2). Interestingly, analysis of the eluates also detected the presence of the small EF-hand protein CALML4 (Fig. 2). Importantly, beads coated with ΔEC1-CDHR5 ED failed to recover both the known IMAC components and CALML4. To further confirm that CALML4 is recovered using this strategy as a result of its direct association with the IMAC, we attempted to repeat these assays using BBs derived from CACO-2_{BBE} monolayers lacking CDHR2. However, given the key role that CDHR2 plays in BB assembly, we were unable to adequately recover isolated BBs from CDHR2 KD cells due to their highly disorganized nature, which makes them mechanically fragile (Fig. S2*A*) (4). We therefore chose to use CDHR2 KD whole-cell lysates as the starting material for these pull-downs. Pull-downs using the CDHR5 ED–coated beads from polarized CDHR2 KD CACO-2_{BBE} cells failed to recover CALML4 (Fig. S2*B*). In contrast, polarized CACO-2_{BBE} cells expressing a negative control (scramble) shRNA resulted in the recovery of CALML4. Together, these data identify CALML4 as a putative component of the IMAC that is associated with the CDHR2 cytoplasmic complex.

CALML4 is found across the human intestinal tract

As a starting point to characterize CALML4 as part of the IMAC, we first set out to identify the CALML4 splice isoforms that are found as transcripts in the intestinal tract. The *CALML4* gene is predicted to encode four different transcript variants in humans. The longest isoform (transcript variant 1) exhibits ~45% amino acid sequence identity to conventional

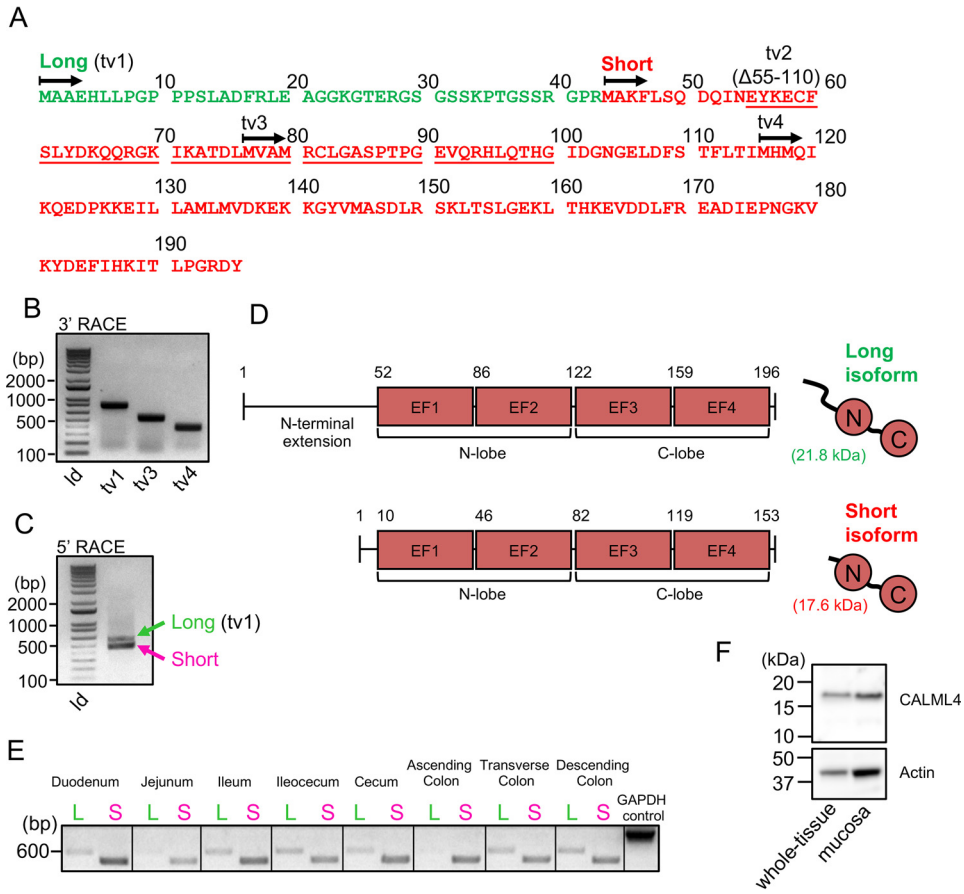

Figure 3. CALML4 transcript is expressed across the human intestinal tract. *A*, sequence of CALML4 showing the four predicted coding transcript variants (*tv*) and the demonstrated "long" (CALML4-L, equivalent to tv1) and "short" (CALML4-S) transcripts identified within the human intestinal tract. *Underlined sequence* shows the region that is spliced out in tv2. The N-terminal extension found in CALML4-L is *green*, whereas CALML4-S is *red*. *B*, DNA agarose gel of 3′ RACE reactions performed using gene specific primers toward the 5′ of tv1, tv3, and tv4. *C*, DNA agarose gel of a 5′ RACE reaction using a gene-specific primer toward the 3′ of CALML4. *D*, *schematic diagram* of the two splice isoform transcripts identified from RACE reactions. *E*, DNA agarose gel of PCRs for the CALML4-L and CALML4-S transcripts across the human intestinal tract. GAPDH is shown as a positive reaction control. *F*, immunoblot analysis for CALML4 and actin using human intestinal whole-tissue and isolated mucosa cell lysates.

calmodulin (Fig. S3*A*) and encodes for a protein 196 amino acids in length that contains an extended N terminus followed by the typical two globular EF-hand–based lobes (denoted here as N-lobe and C-lobe) that are seen with other calmodulin/calmodulin-like protein family members (Fig. 3, *A* and *D*). Proteins encoded by transcript variants 3 and 4 result from utilizing internal start codons compared with transcript variant 1, whereas transcript variant 2 is spliced to remove 47 amino acids internally (Fig. 3*A*). In each case, these shorter variants would encode for CALML4 isoforms that deviate away from the typical bilobed structure by lacking an intact N-lobe. Using gene-specific primers designed against the three different predicted start sites (transcript variants 1, 3, and 4), we performed 3′ RACE against a pool of linker-adapted cDNA derived from human small intestinal tissue (Fig. 3*B*). Cloning and sequencing of the products revealed a common 3′-coding end with no evidence of internal splicing that would be seen with transcript variant 2. We proceeded to perform 5′ RACE using a gene-specific primer toward the 3′ end of CALML4 utilizing the same linker-adapted human intestinal cDNA library. Interestingly, whereas we did detect a minor band that corresponds to the full-length isoform (transcript variant 1), cloning and sequencing of the major product revealed a variant that did not correspond to any of the predicted CALML4 transcripts (Fig. 3*C*). Rather, this transcript utilizes another internal methionine as its start codon and encodes an intact bilobed protein that is identical in sequence compared with transcript variant 1, except that it would lack the N-terminal extension preceding the N-lobe (Fig. 3*D*). We designated the proteins encoded by transcript variant 1 and this novel transcript variant as the "long" and "short" isoforms of CALML4 (referred to as CALML4-L and CALML4-S), respectively (Fig. 3, *A* and *D*).

We investigated the transcript levels of CALML4 across the length of the intestinal tract by screening a human gastrointestinal cDNA panel. We used a primer set specific to CALML4-L and also a set containing a forward oligonucleotide that anneals to the start of the CALML4-S coding sequence. Although the CALML4-S 5′ annealing site is also found in the long isoform, we reasoned that we could gain insight into whether the short isoform transcript is also present in tissues by comparing the relative abundance of long *versus* short isoform product generated in these two reactions. While transcript for the CALML4-L isoform was detected across the entire human intestinal tract, the reaction targeting the CALML4-S sequence consistently gave more product across the entire tissue panel, suggesting that the short isoform is likely the

dominant transcript in the intestine (Fig. 3*E*). Consistent with this, immunoblot analysis for CALML4 using lysates derived from whole tissue and isolated mucosa of human small intestine detected a dominant band at ~17 kDa, which is the predicted size of CALML4-S (Fig. 3*F*). In sum, these data suggest that CALML4 is expressed across the entire human intestinal tract with the short variant likely functioning as the dominant isoform.

CALML4 targets to the tips of BB microvilli

The recovery of CALML4 alongside the other known IMAC components using our purification strategy suggests that CALML4 is a novel IMAC component. To further validate this, we first examined CALML4 localization in mouse intestinal tissue. Confocal imaging revealed high levels of CALML4 in the small intestine (Fig. 4*A*), with signal found in both mature enterocytes on the villus surface and immature cells that reside in the crypt stem-cell niche (Fig. S4*A*). Calculation of the ratio of apical to cytoplasmic signal of CALML4 in enterocytes along the crypt-villus axis demonstrated that CALML4 becomes apically enriched after enterocytes emerge from the crypt domain (Fig. S4*B*). This apical enrichment of CALML4 coincides with development of a prominent BB, as detected using the BB-specific F-actin cross-linking protein, villin (Fig. S4C). Higher-magnification imaging of mature enterocytes revealed striking enrichment of CALML4 at the distal tips of BB microvilli, the site of IMAC function (Fig. 4*A*, *zoom panels*). Line scan analysis of the CALML4 signal along the axis of microvilli revealed an average peak signal at 0.84 ± 0.09 (Fig. 4*B*), when plotted as a function of normalized microvillar length (where 0 = base and 1 = tip). The enrichment of CALML4 in the BB was also evident by immunoblot analysis when comparing a cytosolic protein faction and protein fraction derived from isolated BBs with a prominent band migrating at an approximate molecular mass of ~17 kDa in the BB lysate sample (Fig. 4*C*). This size suggests that that the isoform expressed in mouse intestinal tissue corresponds to the CALML4-S human ortholog.

We further employed stem-derived enteroids and CACO-2_{BBE} cells as intestinal cell culture models to examine the expression and localization of CALML4. In both of these systems, endogenous CALML4 displayed marked enrichment of the distal tips of BB microvilli (Fig. 4, *D* and *E*). We noted that this localization was even retained in isolated BBs derived from polarized CACO-2_{BBE} cells, consistent with the idea that CALML4 was specifically recovered as an IMAC component using our isolation strategy (Fig. 4*F*). To directly examine whether the two splice isoforms of CALML4 exhibit any differences in BB targeting, we created stable CACO-2_{BBE} cell lines expressing CALML4-L and CALML4-S as AcGFP fusion proteins. Both isoforms exhibited identical targeting to the distal tips of BB microvilli, suggesting that the N-terminal extension found specific to CALML4-L does not play a direct role in protein localization (Fig. S4, *D* and *E*). Closer inspection of endogenous and AcGFP-tagged CALML4 targeting in CACO-2_{BBE} monolayers revealed that CALML4 is only apically enriched in cells that have clustering microvilli, indicating that CALML4 is found specially in protrusions that contain active IMAC (Fig. 4*E*; compare *zoom panels 1* and *2* with *panel 3*). Indeed, analysis of the appearance of microvillar clustering relative to endogenous CALML4 expression levels in CACO-2_{BBE} cells revealed a strong positive correlation between these metrics (Fig. 4*G*). Finally, we reasoned that if CALML4 is a component of the IMAC, endogenous CALML4 should colocalize with other IMAC components. Consistent with this prediction, triple labeling of CACO-2_{BBE} monolayers for CDHR2, CALML4, and F-actin showed colocalization of CALML4 with CDHR2 at the tips of clustering microvilli (Fig. 4*H*). Thus, collectively, these data demonstrate that CALML4 is highly enriched in the BB and is positioned correctly at the distal tips of microvilli to be a *bona fide* component of the IMAC.

CALML4 interacts with Myo7b

To begin to shed light on the role of CALML4 within the IMAC, we performed pairwise protein pulldowns of CALML4 with the other known components of this adhesion complex. Pulldown analyses using recombinant cytoplasmic domains of CDHR2 and CDHR5 fused to glutathione *S*-transferase (GST) incubated with COS-7 cell lysates expressing EGFP-tagged CALML4 failed to detect interaction between these components (Fig. S5*A*). Similarly, no interactions were detected between FLAG-tagged CALML4 and any of the domains of the scaffolding molecules USH1C or ANKS4B tagged with Myc and EGFP, respectively (Fig. S5, *B* and *C*). Pulldown analyses did reveal, however, a robust interaction between V5-tagged CALML4 and FLAG-tagged Myo7b. We noted that this interaction did not depend on the presence of calcium (data not shown). Domain mapping studies demonstrated that CALML4 interacts specifically with the neck region of Myo7b and, therefore, may act as a light chain for this myosin (Fig. 5, *A* and *B*). Consistent with this, we noted that the expression of endogenous CALML4 across a polarization time course in CACO-2_{BBE} cells parallels the expression profile of Myo7b, with cellular levels only increasing upon the onset of polarization and BB assembly (Fig. 5*C*). Interestingly, CALML4 was recently reported to be expressed in hair cell epithelia and found to be enriched in stereocilia (25). To investigate whether CALML4 may also function as a direct binding partner for the Usher complex motor, Myo7a, we performed further pulldown analyses using these two molecules. As we observed for Myo7b, V5-tagged CALML4 bound to the neck region of FLAG-tagged Myo7a (Fig. 5*D*). Thus, CALML4 incorporates into the IMAC by function as a light chain for Myo7b (Fig. 5*E*) and may also function as a light chain for Myo7a in stereocilia.

CALML4 targeting to the BB requires Myo7b

Given that we detected an interaction between CALML4 and Myo7b, we investigated whether targeting of CALML4 to the BB depended upon this association. We first assessed the targeting of endogenous CALML4 in CACO-2_{BBE} cell lines that were knocked down (KD) for Myo7b (Fig. S5*D*). In contrast to CACO-2_{BBE} cells stably transduced with a control shRNA, CALML4 failed to accumulate in the BB in Myo7b KD cells (Fig. 5, *F* and *G*). We further explored CALML4 apical targeting using intestinal tissue sections from a Myo7b knockout (KO) mouse. As was observed with our cell culture model, CALML4 was not enriched in the BB of Myo7b KO enterocytes (Fig. 5, *H*

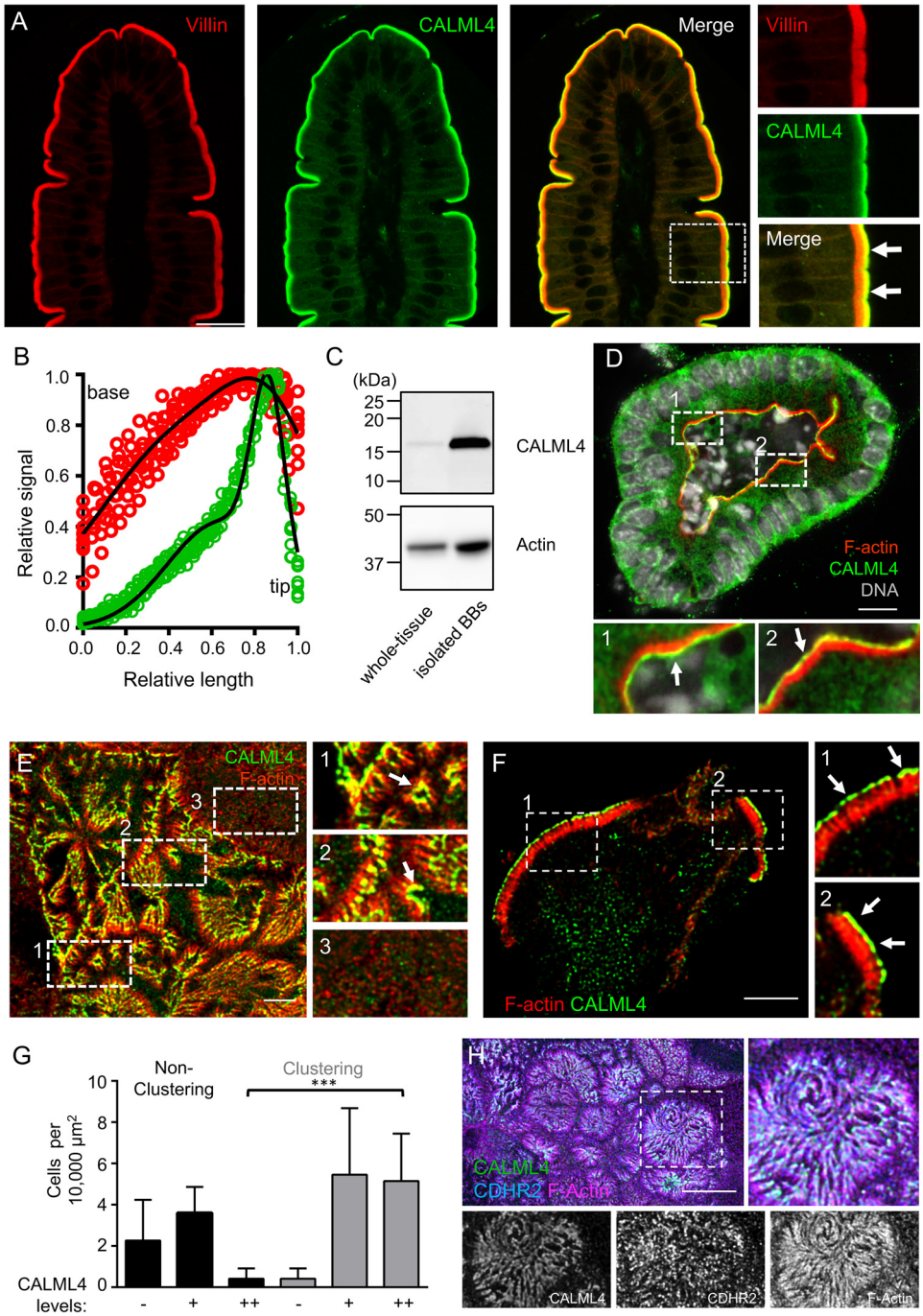

Figure 4. CALML4 localization in native intestinal tissue and enterocyte models. *A*, mouse duodenal tissue stained for CALML4 (*green*) and villin (*red*). The *boxed region* in the *merge* denotes the area in *zooms*. The *arrows* point to CALML4 signal enrichment. *Scale bar*, 20 μm. *B*, line scan analysis of CALML4 (*green*) and villin (*red*) signal intensity parallel to the microvillar axis in mouse duodenal tissue sections. The plot shows a collection of 10 normalized scans taken from three independent immunostaining experiments from tissue sections from three mice. *C*, immunoblot analysis for CALML4 and Actin using protein lysates derived from mouse intestinal whole-tissue samples or isolated mouse BBs (5 μg of total protein loaded). *D*, mouse intestinal organoid stained for CALML4 (*green*), F-actin (*red*), and DNA (*gray*). The *boxed regions* denote the area in *zooms*. The *arrows* point to the CALML4 signal enrichment. *Scale bar*, 20 μm. *E*, 12-day polarized CACO-2_{BBE} cells stained for CALML4 (*green*) and F-actin (*red*). The *boxed regions* denote the area in *zooms*. The *arrows* point to the CALML4 signal enrichment in clustering BB microvilli. *Scale bar*, 20 μm. *F*, isolated BB derived from 21-day polarized CACO-2_{BBE} cells stained for CALML4 (*green*) and F-actin (*red*). The *arrows* point to signal enrichment at the distal tips of microvilli. The *boxed regions* denote the area in *zooms*. *Scale bar*, 5 μm. *G*, quantification of microvillar clustering as a function of endogenous CALML4 levels (n = 412 cells) in 12-day polarized CACO-2_{BBE} monolayers. Data are derived from three independent immunostaining experiments. ***, $p < 0.0001$, t test. *H*, 12-day polarized CACO-2_{BBE} cells stained for CDHR2 (*blue*), F-actin (*magenta*), and CALML4 (*green*). The *boxed region* denotes the area in *zoom*. *Scale bar*, 20 μm. *Error bars*, S.D.

and *I*). Line scan analysis of the distribution of CALML4 along the microvillar axis of Myo7b KO intestinal tissue clearly demonstrated that the small amounts of CALML4 still found in the BB fail to enrich at the microvillar tips in the absence of Myo7b (Fig. 5*J*). Interestingly, CALML4 appears to become slightly enriched at the junctional margins of tissue enterocytes in the absence of endogenous Myo7b (Fig. S5*E*). Together with our protein pulldown data, these studies suggest that CALML4 tar-

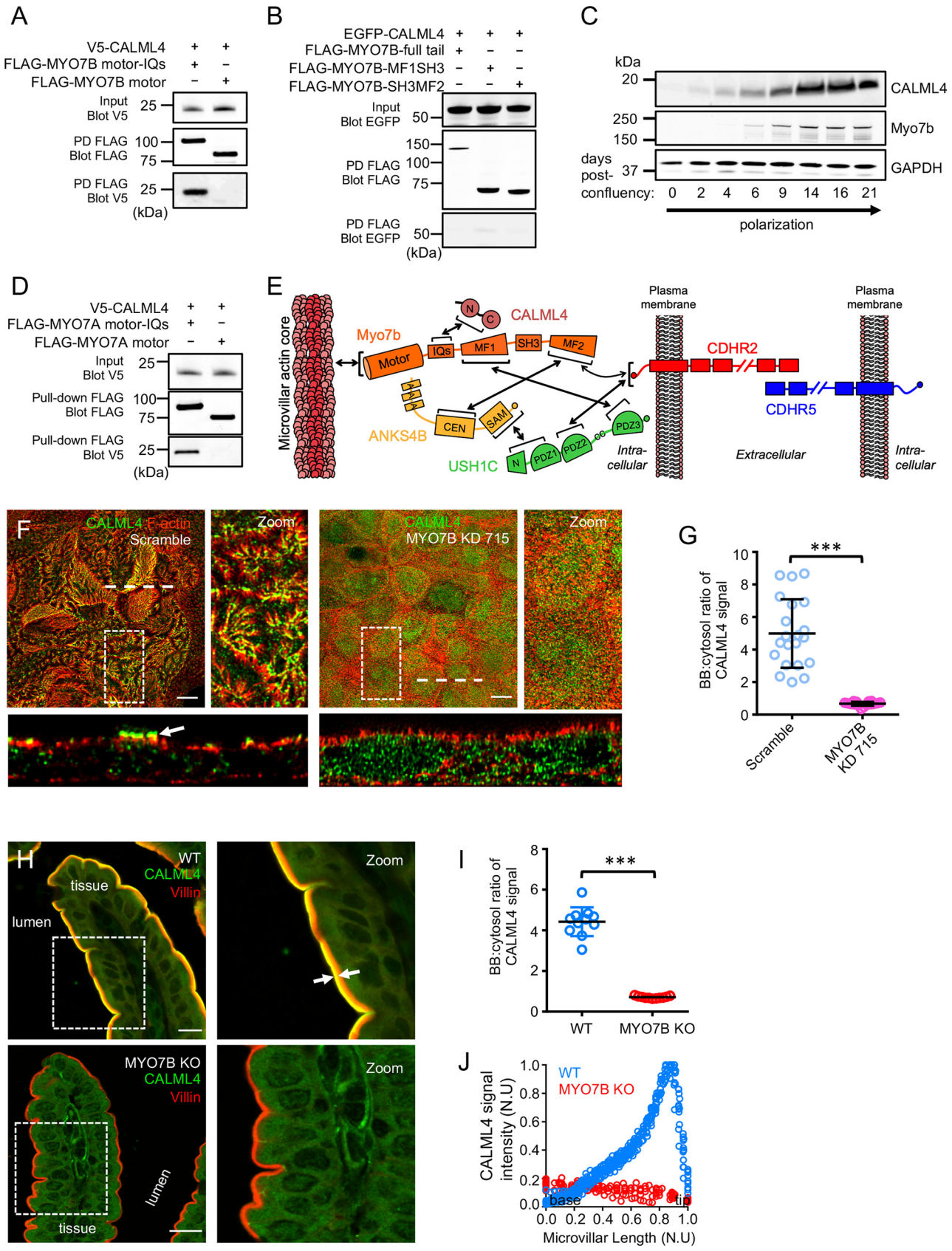
A
V5-CALML4 + +
FLAG-MYO7B motor-IQs + −
FLAG-MYO7B motor − +
Input Blot V5
PD FLAG Blot FLAG
PD FLAG Blot V5
(kDa)
B
EGFP-CALML4 + + +
FLAG-MYO7B-full tail + − −
FLAG-MYO7B-MF1SH3 − + −
FLAG-MYO7B-SH3MF2 − − +
Input Blot EGFP
PD FLAG Blot FLAG
PD FLAG Blot EGFP
(kDa)
C
kDa
CALML4
Myo7b
GAPDH
days post-confluency: 0 2 4 6 9 14 16 21
polarization
D
V5-CALML4 + +
FLAG-MYO7A motor-IQs + −
FLAG-MYO7A motor − +
Input Blot V5
Pull-down FLAG Blot FLAG
Pull-down FLAG Blot V5
(kDa)
E
Microvillar actin core
Myo7b
Motor
IQs
MF1
SH3
MF2
CALML4
ANKS4B
CEN
SAM
USH1C
PDZ1
PDZ2
PDZ3
Plasma membrane
CDHR2
CDHR5
Intra-cellular
Extracellular
Plasma membrane
Intra-cellular
F
CALML4 F-actin
Scramble
Zoom
CALML4
MYO7B KD 715
Zoom
G
BB:cytosol ratio of CALML4 signal
***
Scramble
MYO7B KD 715
H
WT
CALML4
Villin
tissue
lumen
Zoom
MYO7B KO
CALML4
Villin
lumen
tissue
Zoom
I
BB:cytosol ratio of CALML4 signal
***
WT
MYO7B KO
J
CALML4 signal intensity (N.U)
WT
MYO7B KO
base
tip
Microvillar Length (N.U)

gets to the enterocyte BB by directly interacting with the IMAC component Myo7b.

CALML4 is required for normal BB assembly

CACO-2_{BBE} enterocytes serve as a robust model to study the role of the IMAC in BB assembly. Intermicrovillar adhesion leads to the formation of overt clusters of microvilli on the apical surface of CACO-2_{BBE} cells during construction of the BB, providing a readily observable metric of IMAC activity. Importantly, loss of the previously identified components of the IMAC disrupts microvillar clustering and proper BB assembly in this cell line (4, 5, 26). To assess the role of CALML4 in BB assembly, we used lentivirus-mediated transduction to create stable CACO-2_{BBE} shRNA KD cell lines targeting CALML4. We screened four different CALML4 shRNA constructs and identified two independent shRNAs with a KD efficiency above 90% as assessed by immunoblot analysis and immunostaining for CALML4 (Fig. S6, *A* and *B*). Both of these cell lines were allowed to polarize for 12 days past confluence and were then processed to visualize endogenous CALML4 and the F-actin cytoskeleton by confocal microscopy. In both cases, scoring of CACO-2_{BBE} monolayers showed that depletion of endogenous CALML4 resulted in a significant loss of microvillar clustering relative to scramble control cells (Fig. 6, *A* and *B*). Specifically, only ~20% of the cells in CACO-2_{BBE} CALML4 KD monolayers exhibited microvillar clusters, whereas ~70% of WT CACO-2_{BBE} cells had clusters (Fig. 6, *A* and *B*). Importantly, KD of CALML4 in CACO-2_{BBE} cells phenocopies the loss of Myo7b (26). To confirm the specificity of our KD phenotype, we created stable cell lines that reintroduced a refractory EGFP-CALML4 construct into the KD background. We observed that EGFP-positive cells regained the ability to organize their microvilli into well-structured clusters, consistent with the idea that CALML4 is important for IMAC function (Fig. 6, *A* and *B*). In combination with our pulldown data, our results here suggest that CALML4 is a critical light chain for Myo7b and that loss of CALML4 disrupts BB assembly likely through Myo7b dysfunction.

Loss of CALML4 results in mistargeting of other IMAC components

Myo7b has previously been shown to promote targeting of the IMAC to the distal tips of BB microvilli (26). We reasoned that if CALML4 is an obligate light chain required for Myo7b function in CACO-2_{BBE} cells, then loss of CALML4 may also result in defects in IMAC targeting. To assess this, we stained our CALML4 KD cells for individual IMAC components and determined their localization by confocal microscopy. Similar to the loss of Myo7b, KD of CALML4 resulted in significant defects in IMAC targeting (Fig. 7*A* and Fig. S7*A*). When expressed as a ratio of apical to total cell signal, we observed a marked reduction in apical targeting of CDHR2, USH1C, Myo7b, and ANKS4B in our CALML4 KD cells, whereas apical levels of CDHR5 were not significantly affected (Fig. 7*B*). Although rare compared with our scramble control cells, examples of tip targeting for CDHR2, USH1C, Myo7b, and ANKS4B could still be observed in our CALML4 KD cell lines (Fig. 7*A*). The microvilli from CALML4 KD cells that still exhibited tip-targeting of these IMAC components appeared to be organized into rudimentary clusters (see Fig. 7*A*, *zoom panels*), suggesting that some level of IMAC adhesion may still exist in these protrusions. Immunoblot analysis of CALML4 KD cell lysates for the individual IMAC components revealed a trend toward decreased total cellular levels of CDHR2, USH1C, Myo7b, and ANKS4B, whereas CDHR5 was, again, not significantly affected (Fig. 7*C* and Fig. S7*B*). Together, these results are consistent with the premise that CALML4 functions as a critical light chain for Myo7b that is required for efficient targeting of the IMAC to the tips of BB microvilli.

Discussion

CALML4 is a novel IMAC component

In this report, we utilized a protein isolation strategy to enrich for factors that are associated with the cytoplasmic domain of CDHR2. In doing so, we have identified CALML4 as a novel IMAC component. In addition to the fact that CALML4 was discovered using this protocol, the evidence that CALML4 is a *bona fide* component of the IMAC may be summarized as follows: (i) endogenous CALML4 is highly enriched at the tips of BB microvilli in intestinal tissue and CACO-2_{BBE} cells, the site of IMAC function; (ii) when expressed in CACO-2_{BBE} cells, an AcGFP-tagged CALML4 exhibits robust targeting to the tips of BB microvilli; (iii) CALML4 directly interacts with the IMAC component, Myo7b; (iv) BB targeting of CALML4 is strictly dependent upon Myo7b; and finally (v) loss of CALML4 disrupts microvillar clustering, which phenocopies the loss of other IMAC components. We believe that these data provide convincing evidence that CALML4 represents a new, sixth member of the IMAC.

Figure 5. CALML4 localization to the BB requires its association with the neck region of Myo7b. *A* and *B*, mapping the interaction between CALML4 and the subdomains of Myo7b; FLAG-tagged Myo7b constructs served as bait, whereas V5 or EGFP-tagged CALML4 served as prey. *PD*, pulldown. *C*, immunoblot analysis for endogenous CALML4 and Myo7b across a CACO-2_{BBE} differentiation time series. *D*, mapping the interaction between CALML4 and Myo7a; FLAG-tagged Myo7a constructs served as bait, whereas V5-tagged CALML4 served as prey. *E*, domain model summarizing how CALML4 incorporates into the IMAC interactome. *F*, 12-day polarized CACO-2_{BBE} cells stably transduced with either a scramble shRNA or an shRNA targeting Myo7b. Cells are stained for CALML4 (*green*) and F-actin (*red*). The *boxed regions* denote the area in *zooms*. *Dashed lines*, locations where the *x-z* sections were taken; *x-z* sections are shown *below* each *en face* image. The *arrow* points to CALML4 enrichment at the distal tips of BB microvilli. *Scale bar*, 20 μm. *G*, scatterplot quantification of the BB/cytosol ratios of CALML4 signal in scramble and Myo7b KD cell lines. Data points from 20 independent *x-z* sections were taken for each plot, derived from three independent immunostaining experiments. ***, $p < 0.0001$, *t* test. *H*, WT and Myo7b KO mouse duodenal tissue stained for CALML4 (*green*) and villin (*red*). The *boxed region* in the *merge* denotes the area in *zoom*. The *arrows* demarcate CALML4 signal enrichment at the distal tips of BB microvilli. *Scale bar*, 20 μm. *I*, scatterplot quantification of the BB/cytosol ratios of CALML4 signal in enterocytes from WT and Myo7b KO mice. 12 data points were taken from independent images at mid-villus sections for each plot, derived from WT and KO ($n = 3$; ***, $p < 0.0001$, *t* test). *J*, line-scan analysis of CALML4 signal intensity parallel to the microvillar axis in WT and Myo7b KO mice duodenal tissue sections. The plot shows a collection of 10 normalized scans for each line trace, taken from three independent immunostaining experiments using different tissue sections. The microvillar axis has been normalized to 0 = base and 1 = tip (WT and KO, $n = 3$). *N.U.*, normalized units. *Error bars*, S.D.

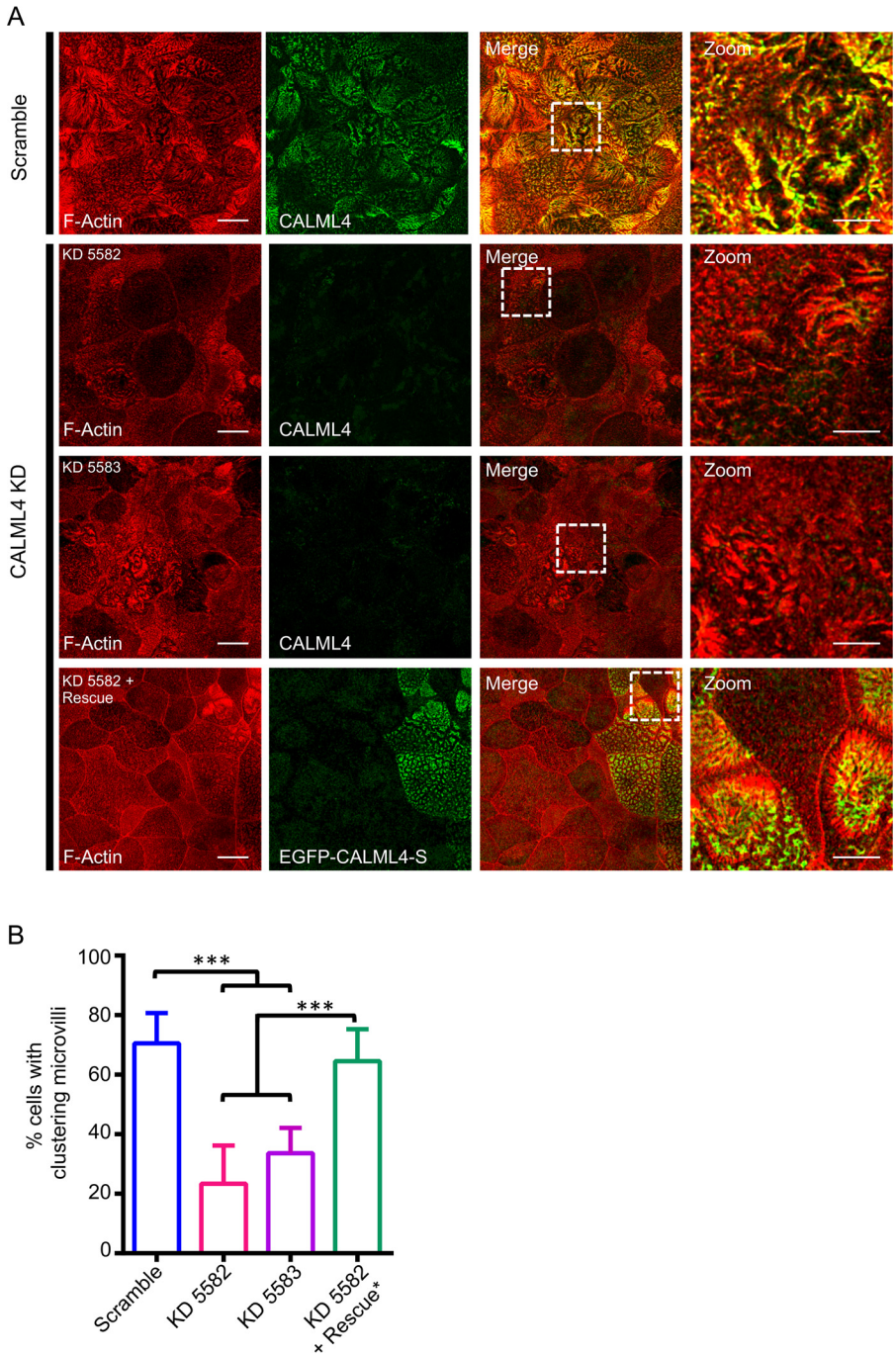

Figure 6. Loss of CALML4 in CACO-2_{BBE} cells disrupts IMAC-mediated microvillar clustering. *A*, 12-day polarized CACO-2_{BBE} cells stably expressing either a scramble shRNA construct or two independent shRNAs targeting CALML4 (KD 5582 and KD 5583), stained for F-actin (*red*) and CALML4 (*green*). The rescue CALML4 KD 5582 line expresses EGFP-CALML4-S that has been made refractory to KD. Rescue cells are stained for F-actin (*red*) and GFP (*green*). The *boxed regions* in *merge images* denote areas in *zooms*. *Scale bars*, 15 μm. *B*, quantification of microvillar clustering in scramble, CALML4 KD, and CALML4 rescue CACO-2_{BBE} cell lines. Only EGFP-positive cells were scored for rescue. Data are from stable cell lines that were independently derived twice (scramble control, $n = 683$ cells; CALML4 KD 5582, $n = 612$ cells; CALML4 KD 5584, $n = 576$ cells; CALML4 KD 5582 refractory rescue EGFP-CALML4-S, $n = 684$ cells). ***, $p < 0.0001$, *t* test. *Error bars*, S.D.

CALML4 functions as a light chain for Myo7b

CALML4 belongs to the calmodulin superfamily of small EF-hand proteins that are known to interact with a diverse set of target proteins that function in numerous cellular pathways. Members of the calmodulin superfamily share the signature "EF-hand" motif, typically found in pairs that constitute a stable structural domain or "lobe" among family members (27). A single EF-hand is a helix-loop-helix motif in which the interhelical loop region positions amino acids that are able to coordinate a calcium ion with a physiologically relevant affinity. This allows members to act as calcium sensors and buffers within the cell (28). In some cases, however, the EF-hands of calmodulin superfamily members have deviated away from the canonical residues involved in calcium ligation, rendering them nonfunctional. These members typically play calcium-insensitive structural roles when bound to their target molecules.

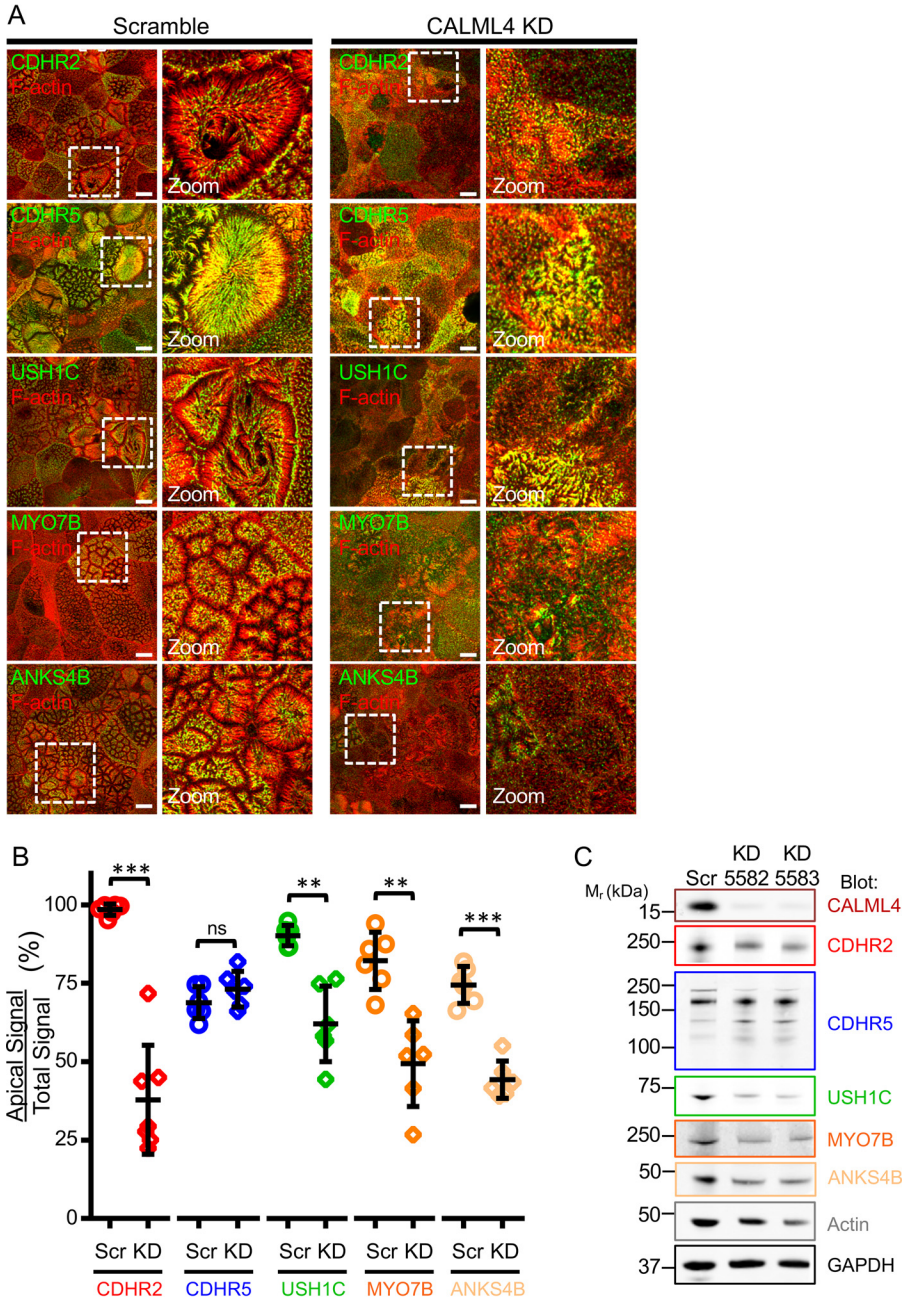

Figure 7. CALML4 is required for normal IMAC localization in CACO-2$_{BBE}$ cells. *A*, 12-day polarized CACO-2$_{BBE}$ cells stably expressing either a scramble shRNA construct or an shRNA targeting CALML4, stained for F-actin (*red*) and either CDHR2, CDHR5, USH1C, Myo7b, or ANKS4B (*green*). The *boxed regions* denote the area in *zooms*. *Scale bars*, 15 μm. *B*, scatterplot quantification of apical/total signal ratios of all of the IMAC components in scramble and CALML4 KD CACO-2$_{BBE}$ cells. Data are from stable cell lines that were independently derived twice. *Data points* are from six independent *x-z* sections taken for each plot. Each *data point* represents the ratio of the entire apical signal found in the *x-z* section compared with the total signal of the *x-z* section. ***, $p < 0.0001$, *t* test; **, $p < 0.001$. *C*, immunoblot analysis of endogenous CALML4, CDHR2, CDHR5, USH1C, Myo7b, ANKS4B, and actin levels in lysates from 21-day polarized scramble control or two independent shRNA CALML4 KD stable CACO-2$_{BBE}$ lines. GAPDH was used as a loading control. *Error bars*, S.D.

Among members of the calmodulin superfamily, CALML4 bears appreciable sequence identity to conventional calmodulin (~45%), while being more distantly related to the other calmodulin-like protein family members (CALML3, 40%; CALML5, 28%; CALML6, 30%). A prominent function of conventional calmodulin is to act as a light chain for members of the myosin family (29). Our domain-mapping studies revealed that CALML4 associates with the neck region of Myo7b, suggesting that it also functions as a myosin light chain. Structurally, light chains function to stabilize the α-helical myosin neck region, thereby allowing the neck to act as a rigid lever arm during force production. In agreement with our findings, previous studies observed that recombinant mouse Myo7a and *Drosophila* Myo7b co-expressed with calmodulin alone (using the baculovirus expression system) purify with substoichiometric amounts of light chain compared with the five IQ motifs found within the neck region of Myo7a and Myo7b. This may indicate that one or more of the IQ motifs in the neck are unoccupied when these myosins are purified under these conditions (30–32). Indeed, the length of the bent conformation of full-

length recombinant *Drosophila* Myo7a observed using EM is less than expected for a motor that has a five-IQ motif lever arm (33). Direct binding studies of recombinant human Myo7a lever arm with calmodulin revealed that it binds two molecules of calmodulin in the absence of calcium and three molecules in the presence of calcium. This further suggests that Myo7a has evolved one or more IQ motifs that recognize a "unique" light chain (32).

Along with playing a structural role in stabilizing the neck region of myosins, light chains can also serve as sites for regulation of myosin activity. Regulation can occur either through light chain phosphorylation or by the direct binding of Ca^{2+} to the light chain. Relevant to our discussion, the motor activity of the Usher complex motor, Myo7a, has been shown to be regulated by Ca^{2+}. Prior to activation, Myo7a exists in an autoinhibited state in which the cargo-binding tail folds back to contact and inhibit the motor-neck region of the myosin (32–34). Whereas the details are still unclear, one mechanism that relieves tail autoinhibition is Ca^{2+} binding to the light chains associated with the neck region of Myo7a. It is not currently known whether Myo7b also exhibits tail-mediated autoinhibition of its motor activity or if its associated light chains have a role in regulating this myosin. It was recently discovered, however, that cargo binding to the tail of Myo7b occurs in an ordered manner, possibly due to the tail being found in an autoinhibited state (5). Whether calcium binding to the light chains associated with the neck region of Myo7b can induce changes in the fold of the tail domain is currently not known. In the future, it will be important to determine whether CALML4 or other light chains play a role in regulating the catalytic or motile properties of Myo7b.

CALML4 in enterocyte BB assembly

We observed that loss of CALML4 results in significant perturbations to BB formation in CACO-2_{BBE} cells. In the absence of CALML4, BB microvilli fail to form organized clusters, suggesting that CALML4 is required for IMAC function. Similar effects are seen with loss of other IMAC components in CACO-2_{BBE} cells, including CDHR2, CDHR5, ANKS4B, and Myo7b (4, 5, 26). In agreement with this, apical levels of CDHR2, USH1C, ANKS4B, and Myo7b are markedly reduced in CALML4 KD cells. Because CALML4 was only detected to interact with Myo7b, it is likely that this effect is due to Myo7b dysfunction. Using a knockdown-rescue approach in CACO-2_{BBE} cells, it was previously shown that only a full-length, motor-active version of Myo7b is able to support normal levels of tip targeting of the IMAC (26). Interestingly, a mutant version of Myo7b (I482A) that has its catalytic activity uncoupled from mechanical force generation was able to support a partial rescue of CDHR2 targeting, suggesting that the ability of Myo7b to function as an actin-binding molecular tether may also contribute to retention of cargoes at microvillar tips independent of force generation (26, 35). Indeed, whereas the overall levels of CDHR2, USH1C, ANKS4B, and Myo7b in the absence of CALML4 were reduced, we did note that discrete examples of tip targeting for these IMAC components could still be seen in our CALML4 KD cell lines. This suggests that if Myo7b does target the IMAC to the distal tips of microvilli using an active transport process, it may still possess low-level motility in the absence CALML4, or there may be other light chains that can compensate for the loss of CALML4. Alternatively, Myo7b may still be able to function as a molecular tether to localize cargo to the microvillar tips without CALML4. Mapping the particular IQ motif(s) with which CALML4 associates within the neck region of Myo7b will be informative toward understanding if CALML4 is an obligate light chain for Myo7b or whether other light chains can partially compensate for the loss of CALML4.

CALML4: a USH1H candidate gene

Deleterious mutations in Usher complex components result in USH1, the most common form of deafness-blindness in humans, affecting ~6/100,000 people in the general population (36). Whereas most USH1 patients only suffer from deafness-blindness, it was noted early on that some patients with mutations in the scaffold USH1C also present with severe inflammatory enteropathy and nephropathy (11, 37). The discovery that USH1C is a shared component of the IMAC and Usher complex provided an explanation for the transporting epithelia dysfunction exhibited by these patients (4). Our study here potentially identifies CALML4 as the second component shared genetically between the IMAC and Usher complex. Consistent with this, CALML4 was previously reported to be highly expressed in hair cell epithelia with a particular enrichment in stereocilia and was also found as part of an immunoaffinity-isolated fraction of stereocilia proteins that associate with Myo7a (25). Furthermore, *CALML4* is one of 27 candidate genes found within the genetic region mapped to contain the causative allele for USH1H, a variant of type 1 Usher syndrome in which the gene responsible has not yet been identified (17). If *CALML4* is the USH1H gene, we would predict that USH1H patients suffer neurosensory deficits due to a dysregulation of Myo7a and may also have undiagnosed gut problems. Interestingly, there are known point mutations within the neck region of Myo7a that cause USH1 (38), lending support to the idea that myosin dysregulation can occur as a result of mutations that disrupt myosin heavy chain–light chain interaction. Going forward, it will be imperative to investigate the localization and localization determinants of CALML4 in hair cells and to determine whether or not CALML4 is the gene responsible for USH1H.

Experimental procedures

Animal model

Details on generation of the Myo7b KO mouse line can be found under RRID:MGI_5757392. Exons between 32013021 and 32014869 of chromosome 18 were deleted to generate the Myo7b null mouse.

Cell culture conditions

CACO-2_{BBE} (male), COS-7, HEK293T, and HEK293FT cells were cultured at 37 °C and 5% CO_2 in Dulbecco's modified Eagle's medium with high glucose and 2 mM L-glutamine (Sigma–Aldrich). Medium was supplemented with 20% FBS (Gibco) for CACO-2_{BBE} cells and 10% FBS for COS-7 and HEK293FT cells. Cell lines were regularly checked with the LookOut Mycoplasma PCR Detection Kit (Sigma–Aldrich).

Table 1
Oligonucleotide sequences

Oligonucleotide	Sequence
5′ and 3′ RACE	
CALML4 tv1 (LONG)	5′-ATGGCAGCCGAGCATTTATTACCCGG-3′
CALML4 tv3	5′-ATGGTGGCCATGAGGTGCCTG-3′
CALML4 tv4	5′-ATGCACATGCAAATAAAACAAG-3′
CALML4 3′	5′-GCGGCCGCCCCTTTCAATAGTCC-3′
Adaptor primer 1 (RACE kit)	5′-CCATCCTAATACGACTCACTATAGGGC-3′
Human digestive system MTC panel PCR screening	
CALML4 tv1 (LONG)	5′-ATGGCAGCCGAGCATTTATTACCCGG-3′
CALML4-S (SHORT)	5′-ATGGCCAAGTTTCTTTCCCAAGACC-3′
CALML4 3′	5′-GCGGCCGCCCCTTTCAATAGTCC-3′
CALML4 K_D shRNA refractory silent mutations	
CALML4 RF5582 sense	5′-TTCTTTCTTTGGGTCTTCTTGTTTGATCTGCATGTGCATAATGGTCAGAAAA-3′
CALML4 RF5582 antisense	5′-TTTTCTGACCATTATGCACATGCAGATCAAACAAGAAGACCCAAAGAAAGAA-3′

Molecular biology

The human cDNA constructs used in this study are as follows: CALML4 (GI: 110227593), ANKS4B (GI: 148664245), USH1C (GI: 225690577), Myo7b (GI: 122937511), CDHR2 (GI: 285002213), CDHR5 (GI: 285002197), and Myo7a (GI: 189083797). DNA encoding these components were generated by PCR and TOPO cloned into the pCR8 entry vector (Thermo Fisher Scientific). The domain boundaries for the Myo7b constructs used are as follows: Myo7b Motor (aa 1–779), Myo7b Motor-IQs (aa 1–893), Myo7b full-length tail (aa 916–2116), Myo7b MF1SH3 (aa 916–1542), and Myo7b SH3MF2 (aa 1501–2116). The domain boundaries for the ANKS4B constructs used are as follows: ANKS4B ANKR (aa 1–252), ANKS4B CEN (aa 253–346), ANKS4B SAM (aa 348–417), ANKS4B ANKRCEN (aa 1–346), and ANKS4B CENSAM (aa 253–417). The domain boundaries for the USH1C constructs used are as follows: NPDZ1 (aa 1–193), PDZ2 (aa 194–295), PDZ2CC (aa 194–451), PDZ3 (aa 379–553), CCPDZ3 (aa 94–553), NPDZ12 (aa 1–302), and PDZ2CCPDZ3 (aa 194–553). The domain boundaries for the Myo7a constructs used are as follows: Myo7a Motor (aa 1–741), Myo7a Motor-IQs (aa 1–876), Myo7a full-length tail (aa 965–2215), Myo7a MF1SH3 (aa 965–1687), and Myo7a SH3MF2 (aa 1603–2215). The protocadherin constructs used in this study are as follows: ectodomain of CDHR5 (residues 1–472), ΔEC1-CDHR5 ectodomain (residues 1–472, Δ27–119), cytoplasmic domain of CDHR5 (residues 697–845), and cytoplasmic domain of CDHR2 (residues 1178–1310). The pLVX-AcGFP-C1 lentiviral vector (Takara) was adapted to Gateway technology using the Gateway Conversion kit (Thermo Fisher Scientific) to generate pLVX-AcGFP-C1-GW. This vector was used for the generation of the stable cell line expressing AcGFP-CALML4. The pINDUCER20 lentiviral vector (39) was modified to include an EGFP tag downstream of the Gateway recombination cassette, to create pINDUCER20-EGFP-N1. This vector was used for the generation of stable cell lines expressing PCDH24-EGFP fusion protein. Vectors used for expression of FLAG, Myc, Fc, and V5-tagged proteins in this study have been described previously (4, 5). Gateway LR reactions were performed using LR Clonase II Plus mix (Thermo Fisher Scientific) according to the manufacturer's instructions and were transformed into DH5-α cells for screening (Thermo Fisher Scientific). Constructs used for the bacterial expression of the cytoplasmic domains (CDs) of the protocadherins have been described previously (4). RACE reactions were performed using the Human Small Intestine Marathon-Ready cDNA kit (Takara) according to the manufacturer's instructions. Screening of the Human Digestive System MTC Panel (Takara) was performed according to the manufacturer's instructions. Knockdown shRNA clones targeting CALML4 and CDHR2 were expressed in the pLKO.1 vector and correspond to TRC clones TRCN0000365582 and TRCN0000365583 for CALML4 and TRCN0000117862 and TRCN0000117865 for CDHR2 (Open Biosystems). A nontargeting scramble control shRNA was expressed from the pLKO.1 vector (Addgene; plasmid 1864).

Oligonucleotide sequences

Oligonucleotide sequences for 5′ and 3′ RACE, MTC panel PCR screening, and CALML4 KD shRNA refractory silent mutations are listed in Table 1.

Lentivirus and stable cell line generation

Lentivirus particles were generated by co-transfecting HEK293FT cells (T75 flasks at 80% confluence) with 6 μg of pLVX-AcGFP-CALML4 or pINDUCER20-PCDH24-EGFP overexpression plasmid with 4 μg of psPAX2 packaging plasmid (Addgene #12260) and 0.8 μg pMD2.G envelope plasmid (Addgene #12259) using polyethyleneimine reagent (Polysciences). Cells were incubated with transfection medium for 12 h, after which they were exchanged with fresh medium. Cells were subsequently incubated for 2 days to allow for lentiviral production. Medium containing lentiviral particles was collected and filtered, and lentiviral particles were concentrated with the addition of Lenti-X concentrator reagent (Takara). For lentivirus transduction, CACO-2_{BBE} cells were grown to 90% confluence in T25 flasks. Prior to lentiviral infection, the medium was supplemented with 8 μg/ml polybrene (Sigma–Aldrich). After 12 h of incubation with lentivirus, the cells were reseeded into T75 flasks and grown for 3 days. Cells were then reseeded into T182 flasks with medium containing 50 μg/ml puromycin (Santa Cruz Biotechnology) or 1 mg/ml G418 (Santa Cruz Biotechnology) and passaged to select for stable integration. Intestinal organoids were generated from mice and processed for immunostaining as described previously (40).

Protein production

To produce recombinant ectodomain fusion proteins, HEK293T cells were grown in T182 flasks to 90% confluence

and transfected with polyethyleneimine reagent (Polysciences) according to the protocol outlined by the manufacturer. Cells were allowed to recover for 12 h, after which the medium was replaced with serum-free Dulbecco's modified Eagle's medium/F-12 supplemented with 2 mM L-glutamine. Cells were then grown for an additional 48 h to allow protein expression into the medium. Medium containing the secreted fusion protein was recovered, filtered, and concentrated using an Amicon Ultra-15 centrifugal filter unit (EMD Millipore). Media containing recombinant ectodomain Fc-fusion proteins were incubated with 20 μl (settled bed volume) of Dynabeads Protein A magnetic beads (Thermo Fisher Scientific) that had been equilibrated in Hanks' balanced saline solution. Beads were washed three times in Hanks' balanced saline solution to remove unbound ectodomain Fc-fusion protein and then directly used in assays. For pulldown assays using GST fusions of the CDs of CDHR2 and CDHR5, constructs were transformed into BL21(DE3) bacteria (Thermo Fisher Scientific), expressed, and purified using GSH resin using standard conditions.

Ectodomain bead cell adhesion assay

CACO-2_{BBE} cells stably expressing CDHR2-EGFP were seeded into coverslips placed into 6-well dishes at a density of 100,000 cells/well. Cells were observed until a confluent monolayer was achieved that marked "day 0." Cells were then allowed to polarize for 6 days, after which 10 μl (settled bed volume) of either CDHR5– or ΔEC1-CDHR5 ectodomain–coated magnetic beads were added to each well. Cells were then allowed to polarize for an additional 6 days, after which they were placed in a coverslip rack to hold them at a 90° angle and washed with 6 × 30 ml of PBS, with gentle rocking agitation for 5 min between PBS changes. Coverslips were subsequently processed either for immunofluorescent imaging or scanning EM.

BB isolation, BB staining, and IMAC recovery

BBs were isolated from rat small intestinal tissue using protocols described previously (41, 42). For BB isolation from cultured cells, CACO-2_{BBE} cells were seeded into four 10-cm^2 dishes at a density of 3×10^6 cells/dish and observed until a confluent monolayer was achieved which marked "day 0." The cells were then allowed to polarize for 21 days, with the medium being swapped every 3–4 days. Cells were then washed once with warm PBS, collected in 10 ml of warm PBS per plate by cell scrapping, combined, and recovered by centrifugation at 500 × *g* at room temperature. The recovered cell volume was noted, and the materials were transferred to an ice bucket. The material was resuspended by pipetting in 10 volumes of cold BB lysis buffer (20 mM imidazole, pH 7.2, 4 mM EDTA, 1 mM 4-benzenesulfonyl fluoride hydrochloride plus one tablet of Roche Protease Inhibitor mixture per 10 ml of volume). The material was then Dounce-homogenized on ice for 30–40 strokes, after which it was transferred to a prechilled conical tube and spun at 3300 × *g* at 4 °C for 15 min. The recovered pellet was resuspended in fresh cold BB lysis buffer and spun at 3300 × *g* at 4 °C for 15 min. Materials after this step were used for either immunostaining or IMAC recovery experiments. For immunostaining of BBs, material was then resuspended in 1 ml of blocking solution (1:1 mix of BB lysis buffer and 5% BSA) for 30 min. Material was recovered by spinning at 3300 × *g* at 4 °C for 5 min in a cooling tabletop centrifuge. The recovered pellet was resuspended in BB blocking solution (500 μl) with primary antibody and incubated for 1 h on ice. Material was then recovered by spinning at 3300 × *g* at 4 °C for 5 min and washed four times with 1 ml of blocking solution. After recovery, material was resuspended in blocking solution (500 μl) containing the appropriate secondary antibody along with Alexa Fluor 568 phalloidin and incubated for 30 min on ice. Material was then recovered and washed as above and finally resuspended in a 1:5 mix of BB lysis buffer/Prolong diamond (~600–800-μl total volume). This mixture was then applied at ~100 μl/glass slide with a syringe and needle (a few drops per slide) and a coverslip mounted on top. Gentle pressure was applied to the coverslip to remove excess sample under coverslip, after which the coverslip was sealed with nail polish, and samples were imaged. For the recovery of the IMAC from isolated BBs, BB material was spun at 3300 × *g* at 4 °C for 5 min and then resuspended in 2 ml of cold Hanks' buffered saline supplemented with 2 mM EDTA and incubated with 20 μl (settled bed volume) of either CDHR5– or ΔEC1-CDHR5 ectodomain–coated magnetic beads for 20 min on a rocking platform at 4 °C. After incubation, 5 mM $CaCl_2$ was added to the reaction to induce adhesion bond formation between the beads and the isolated BBs. The BB/bead mixture was incubated for 20 min on a rocking platform at 4 °C. The beads were subsequently recovered using the DynaMag-2 Magnet apparatus (Thermo Fisher Scientific), washed four times with 1 ml of cold extraction buffer (20 mM Tris, pH 7.5, 150 mM NaCl, 1% Nonidet P-40, 0.5% sodium deoxycholate, 0.05% SDS, 2 mM $MgCl_2$, 2 mM ATP), and eluted with 150 μl of 2× SDS sample buffer at room temperature. Eluates were separated on 4–12% BisTris gels (Novex), and Western blot analysis was performed using the following antibody dilutions: anti-human IgG (Fc-specific) antibody (1:1000; Sigma–Aldrich, catalog no. I2136), anti-CALML4 (1:200; Proteintech 15894-1-AP), anti-ANKS4B (1:200; Sigma–Aldrich catalog no. HPA043523), anti-CDHR5 (1:100; Sigma–Aldrich catalog no. HPA009081), anti-CDHR2 (1:25; Sigma–Aldrich catalog no. WH0054825M1), anti-USH1C (1:250; Sigma–Aldrich catalog no. HPA027398), and anti-Myo7b (1:100; Sigma–Aldrich catalog no. HPA039131).

Microscopy

Cells and tissue sections were imaged using a Leica SP8 or Nikon A1R laser-scanning confocal microscope. Superresolution microscopy was performed using a GE Healthcare/Applied Precision DeltaVision OMX. Scanning EM was performed using a Quanta 250 Environmental scanning EM operated in high-vacuum mode with an accelerating voltage of 5–8 kV. Sample preparation for scanning EM was performed as described previously (4). Paraffin-embedded duodenal tissue sections from WT and MYO7B KO mice were prepared as described previously (4). Samples were stained using anti-CALML4 (1:200; Proteintech 15894-1-AP), anti-Myo7b (1:100; Sigma-Aldrich catalog no. HPA039131), and anti-villin (1:50; Santa Cruz Biosciences, catalog no. sc58897) followed by Alexa Fluor 488 donkey anti-rabbit (1:200; Thermo Fisher Scientific) and Alexa Fluor 568 donkey anti-mouse (1:200; Thermo Fisher

Scientific). CACO-2_{BBE} monolayers were washed once in warm PBS and incubated briefly with 0.02% saponin (Sigma–Aldrich) in warm PBS and then fixed for 15 min with 4% paraformaldehyde (Electron Microscopy Sciences) in warm PBS containing 0.1% Triton X-100 (Sigma–Aldrich). After fixation, cells were washed three times with warm PBS and blocked overnight in a filtered 5% BSA solution. Immunostaining was performed using anti-CALML4 (1:200; Proteintech 15894-1-AP), anti-ANKS4B (1:200; Sigma-Aldrich, catalog no. HPA043523), anti-CDHR5 (1:100; Sigma–Aldrich, catalog no. HPA009081), anti-CDHR2 (1:25; Sigma–Aldrich, catalog no. HPA012569), anti-USH1C (1:250; Sigma–Aldrich, catalog no. HPA027398), anti-Myo7b (1:100; Sigma–Aldrich, catalog no. HPA039131), or anti-GFP (1:200; Aves Labs, catalog no. GFP1020) at 37 °C for 2 h, after which coverslips were washed three times with PBS, and Alexa Fluor 488 donkey anti-rabbit (1:200) secondary antibody or Alexa Fluor 488 goat anti-chicken (1:200) along with Alexa Fluor 568 phalloidin (1:200; Thermo Fisher Scientific) were applied for 1 h at room temperature. Coverslips were then washed five times in PBS and mounted with Prolong Diamond Antifade reagent (Thermo Fisher Scientific). All images shown are *en face* maximum projections through the full height of the BB, with the exception of *x-z* sections, which are single-plane confocal images.

Image analysis

Image analysis was performed using ImageJ (43). For line scan signal analysis, a line was drawn through the BB oriented parallel to the microvillar axis as judged by the villin signal. The intensity of the CALM4 signal along that line was subsequently determined and normalized to the maximum grayscale value for an 8-bit image (*i.e.* 255). The corresponding positions for each intensity value were normalized where the base of the microvillus was equal to 0 and the tip was equal to 1. Normalized line scans were then plotted together and fit to a single Gaussian using nonlinear regression (Prism version 6, GraphPad) to determine the position of peak CALML4 intensity and distribution width ± S.D. relative to the microvillar axis. Image analysis for the ectodomain bead cell adhesion assay was performed in a blinded fashion.

Pulldown assays

For pairwise pulldown assays, COS-7 cells were grown in T75 flasks to 90% confluence and transfected using Lipofectamine 2000 according to the manufacturer's protocol. After 48 h, cells were washed once in warm PBS, recovered using a cell scraper, and lysed in ice-cold Cellytic M buffer (Sigma–Aldrich) containing 2 mM ATP, 1× cOmplete ULTRA protease inhibitor mixture (Thermo Fisher Scientific), and 1 mM Pefabloc SC (Thermo Fisher Scientific). Lysates were centrifuged at 16,000 × *g*, and the soluble fraction was recovered and incubated with a 50-μl bed volume of either pre-equilibrated anti-FLAG M2 resin (Sigma–Aldrich) or GSH resin (Sigma–Aldrich) coupled with GST fused to the CDs of the protocadherins. Resins were incubated with cell lysates for 2 h, rocking at 4 °C; pelleted by a low-speed spin, washed four times using radioimmune precipitation assay buffer (Sigma-Aldrich) supplemented with 2 mM ATP, 1× cOmplete ULTRA protease inhibitor mixture (Thermo Fisher Scientific) and 1 mM Pefabloc SC (Thermo Fisher Scientific); and eluted by boiling in 2× SDS buffer to recover bound material. Resin-bound material was detected by either staining with Coomassie Blue or Western blot analysis with the following antibody dilutions: mouse anti-FLAG M2 (1:1000; Sigma–Aldrich, catalog no. F3165), mouse anti-V5 (1:5000; Thermo Fisher Scientific, catalog no. R960-25), or mouse anti-Myc 9E10 (1:1000; Thermo Fisher Scientific, catalog no. M4439).

Statistical analysis

All graphs were generated and statistical analyses performed using Prism version 6 (GraphPad). For all figures, *error bars* represent S.D. Unpaired *t tests* were employed to determine statistical significance between reported values. Statistical details of individual experiments can be found in figure legends (***, $p < 0.0001$; **, $p < 0.001$; *, $p < 0.01$).

Data availability

All data are contained within the article and supporting information.

Author contributions—M. S. C., M. J. G., S. M., Z. A. S., M. L.W., Z. B. S., and S. W. C. investigation; M. J. T. and S. W. C. funding acquisition; M. J. T. and S. W. C. supervision; M. J. T. and S. W. C. writing-review and editing; S. W. C. conceptualization; S. W. C. data curation; S.W.C. formal analysis; S. W. C. validation; S. W. C. methodology; S. W. C. writing-original draft; S. W. C. project administration.

References

1. Crawley, S. W., Mooseker, M. S., and Tyska, M. J. (2014) Shaping the intestinal brush border. *J. Cell Biol.* **207,** 441–451 CrossRef Medline
2. Barr-Gillespie, P. G. (2015) Assembly of hair bundles, an amazing problem for cell biology. *Mol. Biol. Cell* **26,** 2727–2732 CrossRef Medline
3. Sauvanet, C., Wayt, J., Pelaseyed, T., and Bretscher, A. (2015) Structure, regulation, and functional diversity of microvilli on the apical domain of epithelial cells. *Annu. Rev. Cell Dev. Biol.* **31,** 593–621 CrossRef Medline
4. Crawley, S. W., Shifrin, D. A., Jr., Grega-Larson, N. E., McConnell, R. E., Benesh, A. E., Mao, S., Zheng, Y., Zheng, Q. Y., Nam, K. T., Millis, B. A., Kachar, B., and Tyska, M. J. (2014) Intestinal brush border assembly driven by protocadherin-based intermicrovillar adhesion. *Cell* **157,** 433–446 CrossRef Medline
5. Crawley, S. W., Weck, M. L., Grega-Larson, N. E., Shifrin, D. A., Jr., and Tyska, M. J. (2016) ANKS4B is essential for intermicrovillar adhesion complex formation. *Dev. Cell* **36,** 190–200 CrossRef Medline
6. Pan, L., and Zhang, M. (2012) Structures of usher syndrome 1 proteins and their complexes. *Physiology* **27,** 25–42 CrossRef Medline
7. Jaiganesh, A., Narui, Y., Araya-Secchi, R., and Sotomayor, M. (2018) Beyond cell-cell adhesion: sensational cadherins for hearing and balance. *Cold Spring Harb. Perspect. Biol.* **10,** a029280 CrossRef Medline
8. Sahly, I., Dufour, E., Schietroma, C., Michel, V., Bahloul, A., Perfettini, I., Pepermans, E., Estivalet, A., Carette, D., Aghaie, A., Ebermann, I., Lelli, A., Iribarne, M., Hardelin, J. P., Weil, D., *et al.* (2012) Localization of Usher 1 proteins to the photoreceptor calyceal processes, which are absent from mice. *J. Cell Biol.* **199,** 381–399 CrossRef Medline
9. Schietroma, C., Parain, K., Estivalet, A., Aghaie, A., Boutet de Monvel, J., Picaud, S., Sahel, J. A., Perron, M., El-Amraoui, A., and Petit, C. (2017) Usher syndrome type 1-associated cadherins shape the photoreceptor outer segment. *J. Cell Biol.* **216,** 1849–1864 CrossRef Medline
10. Ahmed, Z. M., Riazuddin, S., Bernstein, S. L., Ahmed, Z., Khan, S., Griffith, A. J., Morell, R. J., Friedman, T. B., Riazuddin, S., and Wilcox, E. R. (2001) Mutations of the protocadherin gene PCDH15 cause Usher syndrome type 1F. *Am. J. Hum. Genet.* **69,** 25–34 CrossRef Medline

11. Bitner-Glindzicz, M., Lindley, K. J., Rutland, P., Blaydon, D., Smith, V. V., Milla, P. J., Hussain, K., Furth-Lavi, J., Cosgrove, K. E., Shepherd, R. M., Barnes, P. D., O'Brien, R. E., Farndon, P. A., Sowden, J., Liu, X. Z., *et al.* (2000) A recessive contiguous gene deletion causing infantile hyperinsulinism, enteropathy and deafness identifies the Usher type 1C gene. *Nat. Genet.* **26,** 56–60 CrossRef Medline
12. Bork, J. M., Peters, L. M., Riazuddin, S., Bernstein, S. L., Ahmed, Z. M., Ness, S. L., Polomeno, R., Ramesh, A., Schloss, M., Srisailpathy, C. R., Wayne, S., Bellman, S., Desmukh, D., Ahmed, Z., Khan, S. N., *et al.* (2001) Usher syndrome 1D and nonsyndromic autosomal recessive deafness DFNB12 are caused by allelic mutations of the novel cadherin-like gene CDH23. *Am. J. Hum. Genet.* **68,** 26–37 CrossRef Medline
13. Bolz, H., von Brederlow, B., Ramírez, A., Bryda, E. C., Kutsche, K., Nothwang, H. G., Seeliger, M., del C-Salcedó, C. M., Vila, M. C., Molina, O. P., Gal, A., and Kubisch, C. (2001) Mutation of CDH23, encoding a new member of the cadherin gene family, causes Usher syndrome type 1D. *Nat. Genet.* **27,** 108–112 CrossRef Medline
14. Verpy, E., Leibovici, M., Zwaenepoel, I., Liu, X. Z., Gal, A., Salem, N., Mansour, A., Blanchard, S., Kobayashi, I., Keats, B. J., Slim, R., and Petit, C. (2000) A defect in harmonin, a PDZ domain-containing protein expressed in the inner ear sensory hair cells, underlies Usher syndrome type 1C. *Nat. Genet.* **26,** 51–55 CrossRef Medline
15. Weil, D., Blanchard, S., Kaplan, J., Guilford, P., Gibson, F., Walsh, J., Mburu, P., Varela, A., Levilliers, J., and Weston, M. D. (1995) Defective myosin VIIA gene responsible for Usher syndrome type 1B. *Nature* **374,** 60–61 CrossRef Medline
16. Weil, D., El-Amraoui, A., Masmoudi, S., Mustapha, M., Kikkawa, Y., Lainé, S., Delmaghani, S., Adato, A., Nadifi, S., Zina, Z. B., Hamel, C., Gal, A., Ayadi, H., Yonekawa, H., and Petit, C. (2003) Usher syndrome type I G (USH1G) is caused by mutations in the gene encoding SANS, a protein that associates with the USH1C protein, harmonin. *Hum. Mol. Genet.* **12,** 463–471 CrossRef Medline
17. Ahmed, Z. M., Riazuddin, S., Khan, S. N., Friedman, P. L., Riazuddin, S., and Friedman, T. B. (2009) USH1H, a novel locus for type I Usher syndrome, maps to chromosome 15q22–23. *Clin. Genet.* **75,** 86–91 CrossRef Medline
18. Jaworek, T. J., Bhatti, R., Latief, N., Khan, S. N., Riazuddin, S., and Ahmed, Z. M. (2012) USH1K, a novel locus for type I Usher syndrome, maps to chromosome 10p11.21-q21.1. *J. Hum. Genet.* **57,** 633–637 CrossRef Medline
19. Chaïb, H., Kaplan, J., Gerber, S., Vincent, C., Ayadi, H., Slim, R., Munnich, A., Weissenbach, J., and Petit, C. (1997) A newly identified locus for Usher syndrome type I, USH1E, maps to chromosome 21q21. *Hum. Mol. Genet.* **6,** 27–31 CrossRef Medline
20. Li, J., He, Y., Weck, M. L., Lu, Q., Tyska, M. J., and Zhang, M. (2017) Structure of Myo7b/USH1C complex suggests a general PDZ domain binding mode by MyTH4-FERM myosins. *Proc. Natl. Acad. Sci. U.S.A.* **114,** E3776–E3785 CrossRef Medline
21. Yu, I. M., Planelles-Herrero, V. J., Sourigues, Y., Moussaoui, D., Sirkia, H., Kikuti, C., Stroebel, D., Titus, M. A., and Houdusse, A. (2017) Myosin 7 and its adaptors link cadherins to actin. *Nat. Commun.* **8,** 15864 CrossRef Medline
22. Marjoram, R. J., Guilluy, C., and Burridge, K. (2016) Using magnets and magnetic beads to dissect signaling pathways activated by mechanical tension applied to cells. *Methods* **94,** 19–26 CrossRef Medline
23. McConnell, R. E., Benesh, A. E., Mao, S., Tabb, D. L., and Tyska, M. J. (2011) Proteomic analysis of the enterocyte brush border. *Am. J. Physiol. Gastrointest. Liver Physiol.* **300,** G914–G926 CrossRef Medline
24. Peterson, M. D., and Mooseker, M. S. (1993) An *in vitro* model for the analysis of intestinal brush border assembly. I. Ultrastructural analysis of cell contact-induced brush border assembly in Caco-2BBe cells. *J. Cell Sci.* **105,** 445–460 Medline
25. Morgan, C. P., Krey, J. F., Grati, M., Zhao, B., Fallen, S., Kannan-Sundhari, A., Liu, X. Z., Choi, D., Müller, U., and Barr-Gillespie, P. G. (2016) PDZD7-MYO7A complex identified in enriched stereocilia membranes. *Elife* **5,** e18312 CrossRef Medline
26. Weck, M. L., Crawley, S. W., Stone, C. R., and Tyska, M. J. (2016) Myosin-7b promotes distal tip localization of the intermicrovillar adhesion complex. *Curr. Biol.* **26,** 2717–2728 CrossRef Medline
27. Ikura, M., and Ames, J. B. (2006) Genetic polymorphism and protein conformational plasticity in the calmodulin superfamily: two ways to promote multifunctionality. *Proc. Natl. Acad. Sci. U.S.A.* **103,** 1159–1164 CrossRef Medline
28. Pangrŝiĉ, T., Gabrielaitis, M., Michanski, S., Schwaller, B., Wolf, F., Strenzke, N., and Moser, T. (2015) EF-hand protein Ca^{2+} buffers regulate Ca^{2+} influx and exocytosis in sensory hair cells. *Proc. Natl. Acad. Sci. U.S.A.* **112,** E1028–E1037 CrossRef Medline
29. Heissler, S. M., and Sellers, J. R. (2014) Myosin light chains: teaching old dogs new tricks. *Bioarchitecture* **4,** 169–188 CrossRef Medline
30. Yang, Y., Kovács, M., Xu, Q., Anderson, J. B., and Sellers, J. R. (2005) Myosin VIIB from *Drosophila* is a high duty ratio motor. *J. Biol. Chem.* **280,** 32061–32068 CrossRef Medline
31. Haithcock, J., Billington, N., Choi, K., Fordham, J., Sellers, J. R., Stafford, W. F., White, H., and Forgacs, E. (2011) The kinetic mechanism of mouse myosin VIIA. *J. Biol. Chem.* **286,** 8819–8828 CrossRef Medline
32. Sakai, T., Jung, H. S., Sato, O., Yamada, M. D., You, D. J., Ikebe, R., and Ikebe, M. (2015) Structure and regulation of the movement of human myosin VIIA. *J. Biol. Chem.* **290,** 17587–17598 CrossRef Medline
33. Yang, Y., Baboolal, T. G., Siththanandan, V., Chen, M., Walker, M. L., Knight, P. J., Peckham, M., and Sellers, J. R. (2009) A FERM domain autoregulates *Drosophila* myosin 7a activity. *Proc. Natl. Acad. Sci. U.S.A.* **106,** 4189–4194 CrossRef Medline
34. Umeki, N., Jung, H. S., Watanabe, S., Sakai, T., Li, X. D., Ikebe, R., Craig, R., and Ikebe, M. (2009) The tail binds to the head-neck domain, inhibiting ATPase activity of myosin VIIA. *Proc. Natl. Acad. Sci. U.S.A.* **106,** 8483–8488 CrossRef Medline
35. Henn, A., and De La Cruz, E. M. (2005) Vertebrate myosin VIIb is a high duty ratio motor adapted for generating and maintaining tension. *J. Biol. Chem.* **280,** 39665–39676 CrossRef Medline
36. Lentz, J., and Keats, B. J. B. (2016) Usher syndrome type I. in *GeneReviews®* (Pagon, R. A., Adam, M. P., Ardinger, H. H., Wallace, S. E., Amemiya, A., Bean, L. J. H., Bird, T. D., Ledbetter, N., Mefford, H. C., Smith, R. J. H., and Stephens, K., eds), University of Washington, Seattle, WA Medline
37. Hussain, K., Bitner-Glindzicz, M., Blaydon, D., Lindley, K. J., Thompson, D. A., Kriss, T., Rajput, K., Ramadan, D. G., Al-Mazidi, Z., Cosgrove, K. E., Dunne, M. J., and Aynsley-Green, A. (2004) Infantile hyperinsulinism associated with enteropathy, deafness and renal tubulopathy: clinical manifestations of a syndrome caused by a contiguous gene deletion located on chromosome 11p. *J. Pediatr. Endocrinol. Metab.* **17,** 1613–1621 CrossRef Medline
38. Adato, A., Weil, D., Kalinski, H., Pel-Or, Y., Ayadi, H., Petit, C., Korostishevsky, M., and Bonne-Tamir, B. (1997) Mutation profile of all 49 exons of the human myosin VIIA gene, and haplotype analysis, in Usher 1B families from diverse origins. *Am. J. Hum. Genet.* **61,** 813–821 CrossRef Medline
39. Meerbrey, K. L., Hu, G., Kessler, J. D., Roarty, K., Li, M. Z., Fang, J. E., Herschkowitz, J. I., Burrows, A. E., Ciccia, A., Sun, T., Schmitt, E. M., Bernardi, R. J., Fu, X., Bland, C. S., Cooper, T. A., *et al.* (2011) The pINDUCER lentiviral toolkit for inducible RNA interference *in vitro* and *in vivo*. *Proc. Natl. Acad. Sci. U.S.A.* **108,** 3665–3670 CrossRef Medline
40. Postema, M. M., Grega-Larson, N. E., Neininger, A. C., and Tyska, M. J. (2018) IRTKS (BAIAP2L1) elongates epithelial microvilli using EPS8-dependent and independent mechanisms. *Curr. Biol.* **28,** 2876–2888.e4 CrossRef Medline
41. Miller, D., and Crane, R. K. (1961) A procedure for the isolation of the epithelial brush border membrane of hamster small intestine. *Anal. Biochem.* **2,** 284–286 CrossRef Medline
42. Tyska, M. J., and Mooseker, M. S. (2002) MYO1A (brush border myosin I) dynamics in the brush border of LLC-PK1-CL4 cells. *Biophys. J.* **82,** 1869–1883 CrossRef Medline
43. Schindelin, J., Arganda-Carreras, I., Frise, E., Kaynig, V., Longair, M., Pietzsch, T., Preibisch, S., Rueden, C., Saalfeld, S., Schmid, B., Tinevez, J. Y., White, D. J., Hartenstein, V., Eliceiri, K., Tomancak, P., and Cardona, A. (2012) Fiji: an open-source platform for biological-image analysis. *Nat. Methods* **9,** 676–682 CrossRef Medline